https://doi.org/10.5194/egusphere-2023-1074
Preprint. Discussion started: 6 June 2023

Fragmentation of ice particles: laboratory experiments on graupel-graupel and graupel-snowflake collisions

Pierre Grzegorczyk[1,2], Sudha Yadav[1], Florian Zanger[1], Alexander Theis[3], Subir K. Mitra[1], Stephan Borrmann[1,3], and Miklós Szakáll[1]

[1]Institute for Atmospheric Physics, Johannes Gutenberg University, Mainz, Germany
[2]Laboratoire de Météorologie Physique (UMR6016)/UCA/CNRS, Aubière, France
[3]Particle Chemistry Department, Max Planck Institute for Chemistry, Mainz, Germany,

Correspondence: Miklós Szakáll (szakall@uni-mainz.de)

Abstract. Until now, the processes involved in secondary ice production which generate high concentrations of ice crystals in clouds have been poorly understood. However, collisions that involve rimed ice particles or crystal aggregates have the potential to effectively produce secondary ice from their fragmentation. Unfortunately, there have only been a few laboratory studies on ice-ice collision, resulting in an inaccurate representation of this process in microphysical schemes. To address this issue, experiments were conducted at the Wind tunnel laboratory of the Johannes Gutenberg University, Mainz on graupel-graupel and graupel-snowflake collisions under still air conditions at -15 °C and over water saturation. All fragments resulting from graupel-graupel collisions were collected and investigated by means of a digital optical microscope, while fragments from graupel-snowflake collisions were observed and recorded instantly after collision using a holographic instrument. From these experiments, distributions were obtained for fragment sizes, cross sectional areas and aspect ratios. The results showed a higher number of fragments at lower kinetic energy compared to those presented in the literature. 150 to 600 fragments were observed for graupel-graupel collisions, and 70 to 500 fragments for graupel-snowflake collisions between 10^{-7} and 10^{-5} J. Parametrizations for fragment size distributions are provided with a mode at 75 µm for graupel-graupel collisions and at 400 µm for graupel-snowflake collisions. These results can be used to improve the representation of ice collision breakup in microphysical schemes.

1 Introduction

The microphysical properties of ice particles within mixed phase clouds play a crucial role in numerical cloud models when determining the amount of surface precipitation (Heymsfield et al., 2020; Field and Heymsfield, 2015) and its temporal evolution (Flossmann and Wobrock, 2010). A particularly well known problem is the observed discrepancies between the concentration of ice nucleating particles and ice crystals (Hallett et al., 1978; Hobbs et al., 1980; Mossop, 1985). This suggests that besides the primary ice generation processes of heterogeneous and homogeneous nucleation, other processes are also involved. Currently,

https://doi.org/10.5194/egusphere-2023-1074
Preprint. Discussion started: 6 June 2023

there is a scientific consensus that secondary ice processes (SIPs) are the key mechanisms responsible for the observed discrepancies in ice crystal number concentration (Field et al., 2017). Korolev and Leisner (2020) discussed six SIPs: (1) shattering during droplet freezing, (2) rime splintering (also called Hallett-Mossop process), (3) fragmentation due to ice-ice collision, (4) fragmentation due to thermal shock, (5) fragmentation of sublimating ice crystals, and (6) activation of ice nucleating particles in transient supersaturation (i.e. high supersaturation zones) around freezing drops. In this paper we investigate the fragmentation breakup of ice crystals due to collision (point 4 in the above list). One of the first ground based observations reporting the presence of broken ice crystals that might have undergone fragmentation due to collision dates back to the seventies (Jiusto and Weickmann, 1973; Hobbs and Farber, 1972). Fragmentation of ice particles was also studied by in situ observations such as Schwarzenboeck et al. (2009) where a significant portion of the broken crystals was attributed to natural fragmentation, or by Takahashi (1993) where the presence of high ice concentration was observed. Recently, von Terzi et al. (2022) found that radar signatures can be potentially attributed to ice aggregate collisions in the dendritic growth layer where fragile dendrite crystals grow. Despite the evidence of the existence of this process, only a few laboratory experiments have been performed till date (Vardiman, 1978; Griggs and Choularton, 1986; Takahashi et al., 1995), which introduces uncertainty in parametrizations. According to the parametrization of Phillips et al. (2017), for instance, the fragmentation breakup of ice crystals is often considered as the primary contributor of ice concentration in convective clouds in forecast models (Huang et al., 2022; Karalis et al., 2022). Alternatively, in the parcel model of (Sullivan et al., 2018), the fragmentation breakup produces as much ice as drop shattering and rime splintering. Nonetheless, numerous important factors such as the number, size, and shape of the fragments, dependency on temperature and ice particle habit are not precisely quantified, to accurately represent the ice fragmentation process in the models.

The first ice-ice collision experiment presented in the literature was carried out by Vardiman (1978), who observed freely falling natural ice particles colliding with a metal plate. Based on the change of momentum of the incoming ice particles Vardiman (1978) proposed a theoretical model to derive the number of fragments. In this experiment, five types of ice particles have been employed and their collisions were captured by a high-speed movie camera. The collision experiments revealed the production of numerous fragments in the case of light to moderately rimed spatial crystals, a fragmentation dependency on the degree of riming for dendrites, and an ineffective fragmentation of graupel particles. Based on these observations and mathematical model, Vardiman (1978) suggested that the collision between heavily rimed dendrite and graupel can produce ice fragments of significant amount. However, according to Phillips et al. (2017), these experiments could have been affected by sublimation weakening and the use of a fixed non-ice target could falsify the results.

Griggs and Choularton (1986) studied the fragmentation of rimed ice and crystals in laboratory. In those experiments, freely falling glass beads of different sizes were made to collide with rimed ice or ice crystals growing on a target rod. The results revealed that a rimed structure does not efficiently produce secondary ice. Conversely, collisions between ice crystals and graupel are very likely produce secondary ice by the fragmentation of the crystal's fragile structure. These conclusions are in agreement with those of Vardiman (1978). Furthermore, spontaneous fragmentation of ice crystals due to aerodynamic drag forces was also observed.

https://doi.org/10.5194/egusphere-2023-1074
Preprint. Discussion started: 6 June 2023

The most comprehensive study was carried out by Takahashi et al. (1995) based on the Takahashi (1993) in situ observation of ice crystals in cumulus clouds. The Takahashi (1993) observations explored a high concentration of 60 and 100 µm ice crystals, when both small (< 2 mm) and large (4 mm) graupels were present. The small graupels were observed having stellar ice branches on their surface. Such graupel with fragile branches were also observed recently by Korolev et al. (2022) at low temperatures. Takahashi (1993) hypothesized that the collision between graupel particles can produce fragments resulting from the breakup of the stellar fragile branches growing on the small graupel surface. Takahashi et al. (1995) aimed to experimentally reproduce graupel-graupel collisions in laboratory experiments adopting two ice spheres of 1.8 cm diameter, which were fixed by metal rods as proxies for graupel. While one of the ice spheres was kept stationary to grow by vapor deposition, the other sphere rotated at a speed of 4 ms^{-1} and grew by riming. The two ice spheres were forced to collide with each other, and ice fragments were released. The experiment was repeated for different growth times, temperatures, and collision forces. The results revealed that the number of fragments increases with increasing collision force and time of depositional growth. A maximum of 800 fragments was produced at around -16 °C. This finding supports that the collision of graupel with different types of crystals grown on their surface can produce many secondary ice crystals. However, this laboratory study can be criticized from several aspects. First, the collision kinetic energy (CKE), which is a fundamental quantity that determines the collision outcome of binary particle collisions (e.g. Low and List, 1982; Szakáll et al., 2014; Phillips et al., 2017), was too high in the Takahashi et al. (1995) experiments (Korolev and Leisner, 2020). CKE is calculated as

$$CKE = \frac{1}{2}\frac{m_1 m_2}{m_1 + m_2}(v_2 - v_1)^2 \tag{1}$$

where m_1 and m_2 are the masses, while v_2 and v_1 are the fall velocities of the large and small graupel, respectively. Since the mass of the ice spheres of 1.8 cm in the Takahashi et al. (1995) experiment exceeded by far that of a natural graupel, the CKE resulted in an unnaturally large number of ice crystal fragments (Korolev and Leisner, 2020). Phillips et al. (2017) also highlighted that the ice spheres in the experiment of Takahashi et al. (1995) were not allowed to move during and after the collision, which could artificially increase the number of the fragments produced. It should be noted that crystals located on the ice sphere were growing on a smooth, non-rimed surface without natural airflow, which does not closely represent the case of a freely falling natural graupel.

Owing to the importance of the process and the lack of reliable laboratory data from experiments, in this paper we introduce a new experimental design to reproduce ice particle collisions more accurately. We also present our first results on the fragmentation after graupel-graupel, as well as graupel-snowflake collisions. In our experiments special attention was given to the parameters that might be crucial for the final outcome, namely the fragile structure grown on the ice particle's surface, the collision kinetic energy, and the temperature. Furthermore, the graupels were generated in a way that resembles their growth in the atmosphere, thus, resulting in natural-like particles in terms of size, density, and structure. The experiments were performed inside the Mainz cold room (M-CR) which is a 4 m × 3 m insulated walk-in cold chamber located in the wind tunnel laboratory of the Johannes Gutenberg University of Mainz, Germany. The room temperature was set to -15 °C where fragile dendritic crystals are expected to grow most efficiently.

https://doi.org/10.5194/egusphere-2023-1074
Preprint. Discussion started: 6 June 2023

This paper is organized as follows: in Section 2 the experimental setup and procedures for ice particle generation are described. The setup for ice particle collisions is introduced in section 3, while the results for the fragment number, size and shape are presented and analysed in section 4.

2 Experimental setups for ice particle production

2.1 Generation of nature-like graupel particles

Nature-like graupel were generated by means of the GEORG (GEnerator instrument Of Rimed Graupel) apparatus (see details in Theis et al., 2022). This setup consists of flow tube with a square cross section (17 cm x 17 cm x 200 cm) which is placed inside the M-CR in which a small epoxy spheroid about 1 ± 0.2 mm diameter, mimicking a frozen drop and acts as the embryo for the graupel. The epoxy core is attached to a 40 $\mu\mathrm{m}$ diameter fiber which is fixed to a double gyration apparatus inside the flow tube. This apparatus consists of one electric motor rotating around the vertical axis, and a second one which is fixed at 45° angle with respect to the first one. Both motors are rotating at 4 Hz. simulating the rotation and tumbling motion of a freely falling graupel. The whole surface of the epoxy embryo was exposed this way to a supercooled droplet flux in order to produce a lump graupel (classified as Rb4 in Kikuchi et al., 2013). A constant flow speed of 2.78 ± 0.10 ms^{-1} was produced by a blower on the top of the flow tube to simulate the free fall of the graupel and to maintain a central droplet stream inside the flow tube. Liquid droplets with a modal diameter of 19.7 ± 5.1 $\mu\mathrm{m}$, arithmetic mean diameter of 23.4 ± 8.8 $\mu\mathrm{m}$ and a volume diameter of 34.6 ± 9.9 $\mu\mathrm{m}$ were generated by the means of an ultrasonic atomizer (US 2/58 Hz, Lechler GmbH, Germany) which was fed by 15 mLmin^{-1} input nitrogen gas flux. An ice filter was added at the top of the flow tube to avoid ice accretion inside the blower.

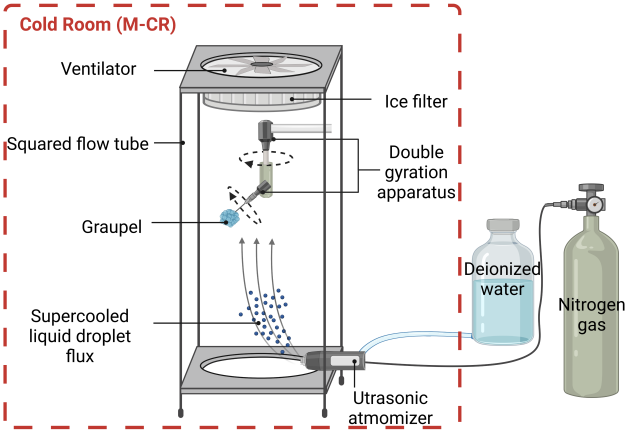

Figure 1. The apparatus GEORG used for the generation of nature-like lump graupel (Theis et al., 2022, modified after). The flow tube was placed inside the M-CR at -15 °C, while the gas and water bottles were kept outside the cold room.

https://doi.org/10.5194/egusphere-2023-1074
Preprint. Discussion started: 6 June 2023

To characterize their mass, each graupel was melted and the size of the resulting liquid drop was measured by following the procedure of Theis et al. (2022). Before melting, each graupel diameter was estimated from microscope images adopting three methods: (1) the equivalent area diameter from the graupel's apparent cross section; (2) two equivalent volume diameters from two estimations of the graupel's volume determined by an elliptical fit on the graupel edges contours; (3) two equivalent volume diameters from an integration method used in Szakáll et al. (2014). The resulting statistics of the mean graupel characteristics is given in Table 1.

Temperature (°C)	LWC (gm^{-3})	Growth time (s)	Number of graupel	Diameter (mm)	Density (gcm^{-3})
-10 ± 1.5	3.46 ± 0.23	180	5	2.43 ± 0.3	492 ± 88
-10 ± 1.5	3.50 ± 0.78	420	2	4.47 ± 0.36	782 ± 166
-15 ± 1.5	2.32 ± 0.16	180	5	2.24 ± 0.17	334 ± 62
-15 ± 1.5	2.20 ± 0.12	360	5	3.51 ± 0.36	510 ± 70
-20 ± 1.5	0.71 ± 0.08	420	5	2.05 ± 0.28	248 ± 23

Table 1. Graupel mean characteristics for different temperatures, growth times and liquid water content (LWC) generated using the GEORG instrument (Fig. 1).

For each graupel, the volume determined by the three previous methods and the mass estimated from the melting were used to calculate its density. For the collision experiments, graupels were generated at -15 ± 1.5 °C under the same conditions as graupel presented in Table 1. The two densities obtained for this temperature are 334 ± 62 gcm^{-3} for the graupel with roughly 2 mm size and 510 ± 70 gcm^{-3} for roughly 4 mm graupel (the choice of graupel size is explained in section 3.1.1). These values for the two densities needed to be used for the calculation of the graupel masses and CKE because melting the graupel after the experiments was not possible.

2.2 Ice crystal growth by water vapor deposition

Dendritic ice crystals were grown on the surface of graupel particles by deposition of water vapor. For that, a glass aquarium setup (Fig. 2.), similar to the one described by Fries et al. (2006) was utilized in the M-CR. At the top of the aquarium, supersaturation with respect to ice was maintained by humidifying the cold dry ambient air with water vapor evaporated from a heated water bath. The water vapor saturation level was determined by the M-CR air temperature and by the water bath temperature which was controlled and stabilized using a heating resistance plate. A homogeneous water bath temperature was ensured by the continuous stirring of the water using a magnetic stirrer. To characterize the crystal growth, two PT-100 sensors were mounted inside the aquarium to measure the air and water temperatures, respectively. The ice supersaturation was determined from the dew point measured by a chilled mirror dew point hygrometer (DP3-D/SH, MBW Elektronik AG, Switzerland) in the immediate vicinity of the growing ice crystals. In order to avoid condensation inside the sampling tube, it was coiled up and heated by a conductive wire dissipating heat.

https://doi.org/10.5194/egusphere-2023-1074
Preprint. Discussion started: 6 June 2023

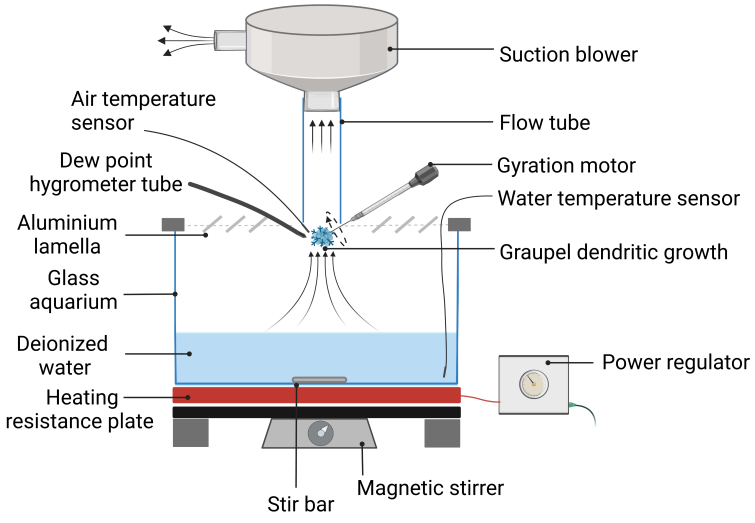

Figure 2. Experimental setup for producing dendritic ice crystals on graupels' surface. See the text for details.

To reproduce graupel with vapor grown crystals on their surface as observed by Takahashi (1993), a 2 mm graupel was held by a fibre inside a cannula over the aquarium on a 4 rpm gyration motor. The motor simulates the rotation of a natural graupel and induces a homogeneous dendritic growth on the graupel surface. A blower and a flow tube were placed above the graupel particle in order to simulate the natural air flow pattern of its fall. The flow speed was set at the position of the graupel to 2.50 $\pm$ 0.25 ms^{-1} which is in the range of a 2 mm diameter graupel's terminal velocity (Heymsfield and Wright, 2014). The temperature of the M-CR was kept at -20.0 $\pm$ 1.5°C which lead to an air temperature at the position of the graupel between -13 and -15 °C. The water bath temperature was set to 13.1 $\pm$ 0.2°C, resulting in a supersaturation over ice between 20 and 27% (Fig. 3).

In a natural cloud with 6.6×10^{-3} $^{\circ}\mathrm{Cm}^{-1}$ temperature gradient, a 2 mm graupel falling at 2.5 ms^{-1} would experience a temperature increase of 5°C within 5 minutes. Hence, such a graupel would stay in the dendritic growth zone between -20°C and -10°C during this time in a cloud without updraft, as observed in Takahashi (1993). Therefore, we allowed 5 minutes growth time of dendritic crystals in our experiments.

In order to verify the ability of our setup to produce realistic cloud ice crystals, the blower was turned off to produce vapor grown ice crystals in still air conditions. In this case, numerous ice crystals were growing on the aluminum plates at the top of the aquarium. These crystals were collected and investigated using an optical microscope in order to characterize their shape following Kikuchi et al. (2013).

Figure 4 provides a comparison of temperature, ice supersaturation and crystal type obtained in our experiments (symbols) with Kobayashi (1961) diagram which is represented by black solid and dotted lines, with a special focus on the dendritic growth zone around -15°C. The Kobayashi (1961) ice crystal diagram has been assessed and found to be in agreement with

https://doi.org/10.5194/egusphere-2023-1074
Preprint. Discussion started: 6 June 2023

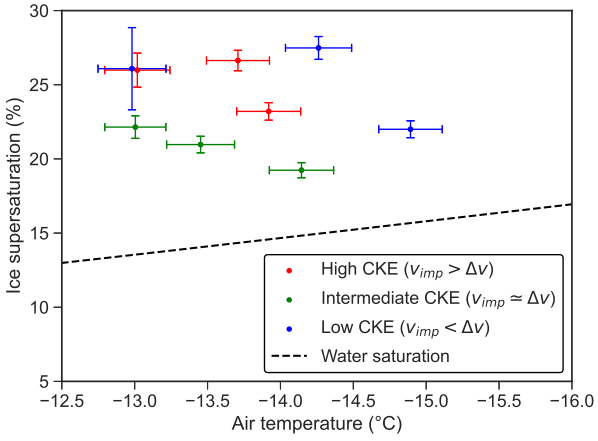

Figure 3. Temperature and ice supersaturation during deposition growth for graupel used in collision experiments (see in Section 4.1). The graupel employed for low CKE experiments are plotted in blue, for intermediate CKE in green, while for high CKE in red (see section 3.1.2).

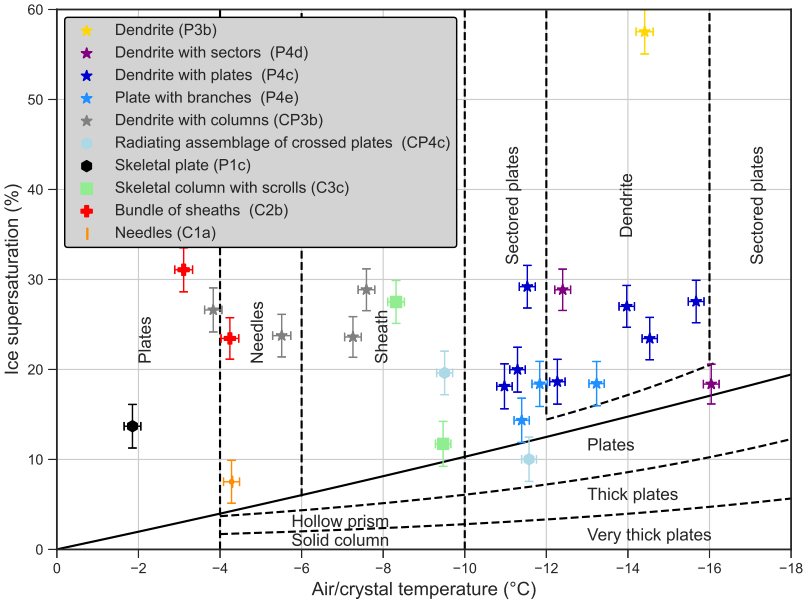

Figure 4. Depositional grown ice crystals inside the aquarium setup categorized following Kikuchi et al. (2013) and compared to Kobayashi (1961) diagram.

other laboratory studies and cloud observations (Pruppacher and Klett, 2010). As demonstrated in Fig. 4 aquarium setup produces ice crystals similar to those expected in the clouds and that its use is appropriate for collisions experiments.

https://doi.org/10.5194/egusphere-2023-1074
Preprint. Discussion started: 6 June 2023

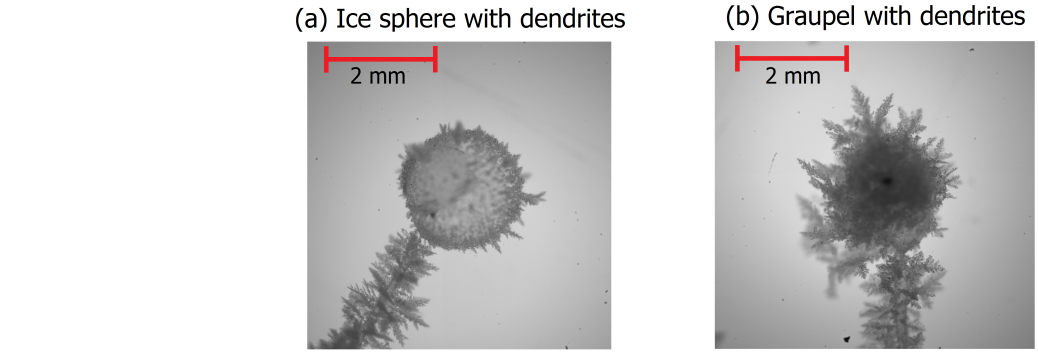

Figure 5. Ice sphere with dendritic crystals similar to Takahashi et al. (1995) and graupel with dendrites used in this study for collisions. For both ice particles, dendritic crystals (around 700 µm maximum dimension for the longest one) are produced after 5 minutes of vapor deposition (T ≈ -14 °C and $S_{ice} \approx 23\%$) by means of the aquarium setup shown in Fig. 2

Figure 5 depicts dendritic ice crystals grown on the surface of an ice sphere and of a graupel particle. The graupel was generated in GEORG at -15°C (see Table 1), while the ice sphere was produced by wet growth, adding successively liquid layers around the ice core and waiting for complete freezing. Dendrites grown on the supporting wires of the two ice particles have similar sizes which demonstrates that the growth of crystals are similar under the same conditions and the same surface of deposition. The maximum size of a dendritic crystal observed in Fig. 5a was approximately 400 µm, and 700 µm in Fig. 5b. The structure of pure ice which was created by wet growth apparently inhibits the growth of dendrites compared to the rough structure of rimed graupel. Since Takahashi et al. (1995) used smooth ice spheres, collision experiments can be different to those where the dendritic growth takes place on rimed (i.e., rougher) surfaces.

3 Collision experiments

3.1 Graupel-graupel collisions

The purpose of the first collision experiments was to reproduce the Takahashi et al. (1995) experiments in a more realistic manner in terms of ice particle size, and to develop an improved method to detect and count the generated ice crystal fragments. Therefore, the decision to select 2 mm and 4 mm graupel sizes for the collision experiments was made based on the particle sizes observed in Takahashi (1993) study, which estimated the expected collision of graupel particles in the atmosphere.

3.1.1 Setup for graupel-graupel collision experiments

Graupel-graupel collisions were performed inside a 4.5 cm diameter "collision tube" as shown in Fig. 6. An additional, 8 mm diameter "drop tube" was placed on the top of the "collision tube" to guide the falling graupel to the impact point. A 2 mm graupel with vapor grown crystals on its surface was carefully and quickly moved from the aquarium to its proper position in

https://doi.org/10.5194/egusphere-2023-1074
Preprint. Discussion started: 6 June 2023

the "collision tube". It was held by a thin wire fitted into a cannula. As this wire possesses only a small aerodynamic resistance, the graupel was allowed to move after collision (see Fig. 7). The 4 mm graupel's supporting wire used for its generation was cut close to its surface and held with tweezers before launching it through the "collision tube". An example of a video recorded during an experiment on graupel-graupel collision is provided as a supplement of this paper (see https://doi.org/10.5446/62064).

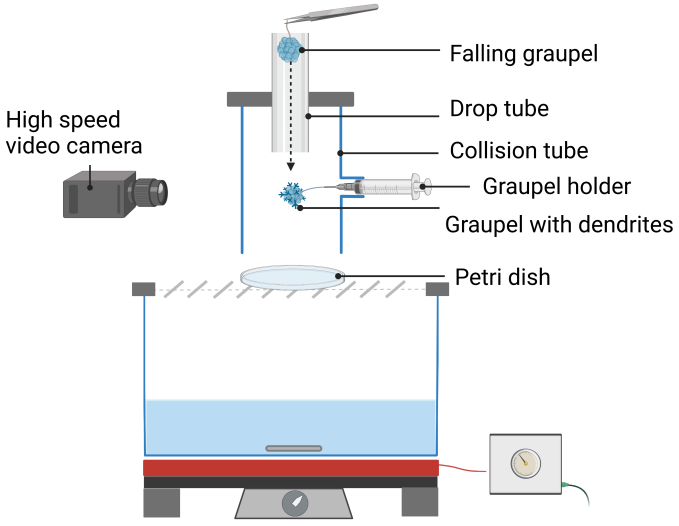

Figure 6. Experimental setup for graupel-graupel collisions over the glass aquarium inside the M-CR

The setup was placed over the glass aquarium to avoid any sublimation weakening of the dendritic crystals. Each collision was captured by a high-speed camera (MotionPro Y3) at 1000 fps. A petri dish filled with a thin layer of paraffin oil ($\rho \approx 0.85 \pm 0.03$ $\mathrm{gcm^{-3}}$) was placed at the bottom of the collision tube to collect the ice fragments generated by the collision. A few seconds after the collision, the petri dish was covered by another layer of paraffin oil previously stored at -5°C. As the cold room temperature was around -20°C, the oil solidified which immobilizes the crystals on the petri dish. After being collected, pictures of fragments were taken and later analysed (see section 3.1.3).

3.1.2 Fall speed and collision kinetic energy

The small graupel with dendrites was fixed in the "collision tube", resulting in a reduction of the terminal velocity difference expressed in the original CKE equation (Phillips et al., 2017) to the fall speed of the large graupel v_1 in Eq. 1. As a result, the CKE is determined by the masses of the graupel particles and the velocity v_1 of the large graupel. However, in natural clouds, both particles would be falling, which implies that v_1 should be equal to the terminal velocity difference of the two graupel particles Δv for our experiment.

https://doi.org/10.5194/egusphere-2023-1074
Preprint. Discussion started: 6 June 2023

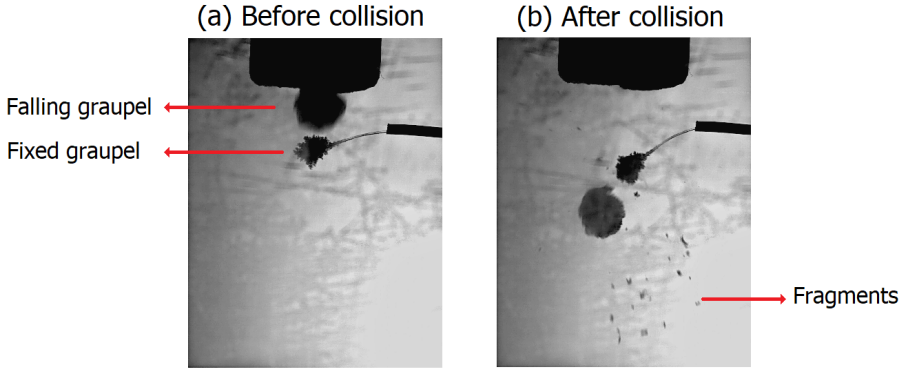

Figure 7. Images of graupel in the collision tube (a) before and (b) after collisions as captured by a high speed camera

From Eq. A9 in Appendix A and a realistic drag coefficient C_d=1 for graupel of the investigated sizes (Heymsfield et al., 2018), the two theoretical graupel terminal velocities are $v_T(D = 4\ \mathrm{mm}\ , \rho_g = 0.51\ \mathrm{gcm^{-3}})$ = $4.36\ \mathrm{m.s^{-1}}$, and $v_T(D = 2\ \mathrm{mm}\ , \rho_g = 0.34\ \mathrm{gcm^{-3}})$ = $2.50\ \mathrm{ms^{-1}}$. The typical terminal velocity difference between these two graupel is therefore Δv=1.86 $\mathrm{ms^{-1}}$. From this typical terminal velocity difference, three tube lengths were chosen (Table 2) depending on the large graupel's velocity just before the collision as expressed in Eqs. A7 and A8. By employing three different falling distances, one can modify the kinetic energy and observe how it impacts the outcomes of collisions. The small tube corresponds to an impact speed $v_1 < \Delta v$, the intermediate tube to $v_1 \simeq \Delta v$ and the long tube to $v_1 > \Delta v$. The three CKE ranges in Table 2 will be

Tube	Tube length (cm)	Calculated v_1 ($\mathrm{ms^{-1}}$)	Measured v_1 ($\mathrm{ms^{-1}}$)	Calculated CKE (J)	Measured CKE (J)
Short tube	5	1.14	1.02 ± 0.15	8.4×10^{-7}	$1.2\times10^{-6} \pm 0.4\times10^{-6}$
Intermediate tube	22	1.86	1.96 ± 0.15	2.2×10^{-6}	$4.7\times10^{-6} \pm 1.3\times10^{-6}$
Long tube	80	3.58	3.06 ± 0.15	8.3×10^{-6}	$1.6\times10^{-5} \pm 0.4\times10^{-5}$

Table 2. Mean graupel fall speeds and CKEs measured (from collisions experiments) or calculated for different collision tube lengths adopting Eqs. A7 and A8. The tube lengths are corresponding to velocity differences of a 2 mm (ρ = $334 \pm 62\ \mathrm{gcm^{-3}}$) and a 4 mm ($\rho$ = $510 \pm 72\ \mathrm{gcm^{-3}}$) graupel.

referred hereinafter as low, intermediate and high CKE. Graupel-graupel collisions were carried out 3 times for each kinetic energy range. For each collision, the CKE was calculated under the above mentioned consideration. Since in our setup it was not possible to melt the graupel after the collisions, its masses was derived from the mean densities from the characterization measurements at -15 °C (see Table 1), and from their volume calculated from their images described in section 2.1. The mass of vapor grown dendritic crystals on the small graupel was neglected. Images recorded by the high speed camera were used to calculate the large graupel's fall speed v_1 with an accuracy of 0.15 $\mathrm{ms^{-1}}$ according to the camera pixel size and frame rate.

https://doi.org/10.5194/egusphere-2023-1074
Preprint. Discussion started: 6 June 2023

3.1.3 Crystal image processing

The ice crystal fragments inside the petri dish were analyzed unsing a microscope. For that, the petri dish surface was subdivided into a $5\mathrm{mm} \times 5\mathrm{mm}$ grid (see Fig. 8a). Microscope pictures of 3.00 µm pixel resolution were taken for each grid cell. Because of the numerous dust particles present in the petri dish, ice fragments were identified manually and contoured on the computer image by red rectangles as shown in Fig. 8b. For each picture, the portions delimited by red rectangles in each grid mesh were selected and counted as a single ice particle (Fig. 8c).

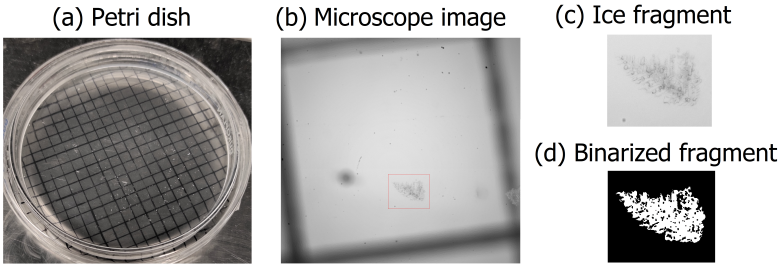

Figure 8. (a) Ice fragments collected after a graupel-graupel collision on the petri dish filled with paraffin oil. (b) Microscope picture of ice fragments inside a grid cell. Image processing steps are shown in (c) and (d).

A double gradient, which consists of summing the intensity gradient of rows and columns of the image pixels, was applied to identify crystal outlines. The gradient pictures were binarized using a threshold value chosen and applied for all images and fragments. Dilatation-and-erosion as morphological closure was applied to fill the holes in the dendritic structure images and get a single crystal. Dust particles inside the red rectangles around the chosen crystals (see Fig. 8c) were automatically filtered out by considering only the largest particle cross sectional area which are ice fragments (see Fig. 8d). From the individual binarized fragments, the major and minor axes were obtained by fitting an ellipse in the same way as for graupel particles (see Section 2.1).

3.2 Graupel-snowflake collisions

Snow crystal aggregates (called snowflakes hereinafter) around 10 ± 2 mm were manually formed by sticking together around 20 to 60 millimeter-size P3b/P4d ice crystal monomers. These dendritic crystals were grown inside the glass aquarium in still air (Fig. 2) using the temperature and humidity conditions provided in Fig. 4 for P3b/P4d crystals. Although the microscope method is utilized to identify fragments in graupel-graupel collisions, it is not suitable for graupel-snowflake collisions due to the overlapping of dendrite fragments in the petri dish, which obstructs their accurate identification. To overcome this issue, the "Holographic Imaging and Velocimetry Instrument for Small Cloud Ice" (HIVIS) Weitzel et al. (2020) was introduced to detect the ice fragments produced by freely falling graupel-snowflake collisions. Consequently, holographic images were captured for the ice fragments generated from graupel-snowflake collisions.

https://doi.org/10.5194/egusphere-2023-1074
Preprint. Discussion started: 6 June 2023

3.2.1 Setup for graupel-snowflake collisions

The collision took place in a transparent tube of 1.9 cm inner diameter and 50 cm length placed above the HIVIS instrument as shown in Fig. 9. A snowflake was placed onto a 1.3 cm × 1.3 cm squared plate mounted on a hinge. Next, the snowflake was launched by turning the hinge, and at the same time, the graupel was starting to fall from a few centimeters above the tube. Since the fall speed of the graupel is higher than that of the snowflake, the collision took place as soon as the graupel overtook the snowflake. As the launch of the snowflake was carried out by the operator, the place where the graupel caught the snowflake was unpredictable. Hence, collisions had different collision kinetic energies depending on the actual velocity difference of the particles at the instant of the collision. Video sequences of central and edge collisions are shown in Fig. 10, while the complete videos of collisions are provided as supplements of this paper (see https://doi.org/10.5446/62066 and https://doi.org/10.5446/62065).

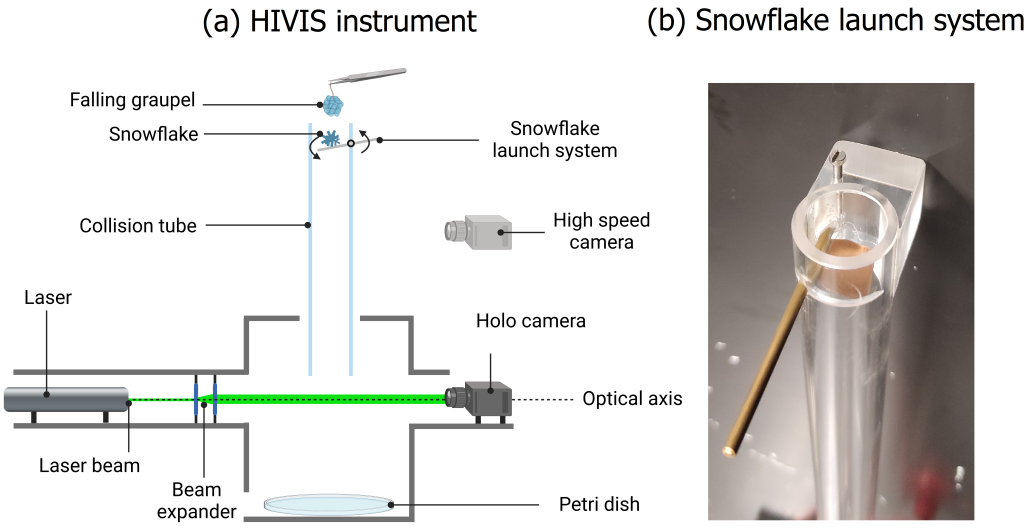

Figure 9. (a) The HIVIS instrument (Weitzel et al., 2020) for graupel-snowflakes collisions inside the M-CR composed and (b) the snowflake launching system.

After the collision, all fragments were falling through the tube toward the sampling volume of the HIVIS instrument and crossed the laser beam. Ice fragment falling through a 2.2 × 2.2 × 4 cm sampling volume were captured by a camera (Basler Ace 2) at 90 fps with a pixel resolution of 10.87 µm. All the fragments were collected in a Petri dish located sufficiently at the bottom of the HIVIS to avoid interfering with the detection of freely falling fragments in the laser sampling volume. The fragments were then melted and weighted to measure the total snowflake mass. The CKE was calculated from this mass and the images recorded at 400 Hz by the high speed camera, which images the entire tube. The graupel can collide with a snowflake at different positions measured from the snowflake's center, which might influence the generated fragment number or size. In

https://doi.org/10.5194/egusphere-2023-1074
Preprint. Discussion started: 6 June 2023

order to investigate this effect, the impact position parameter I_p similar to eccentricity for drop-drop collisions (see Szakáll and Urbich, 2018) is introduced as

$$I_p = 1 - \frac{x_g - x_s}{R_s} \tag{2}$$

where x_g and x_s are the apparent horizontal center position of the graupel and the snowflake, respectively, and R_s is the radius of the snowflake calculated as half of the snowflake maximum dimension. In case of central collision $I_p = 1$ (Fig. 10a), while for edge collision $I_p = 0$ (Fig. 10b). This parameter is calculated from the pictures of only one camera point of view which imposes limits to the precision of I_p.

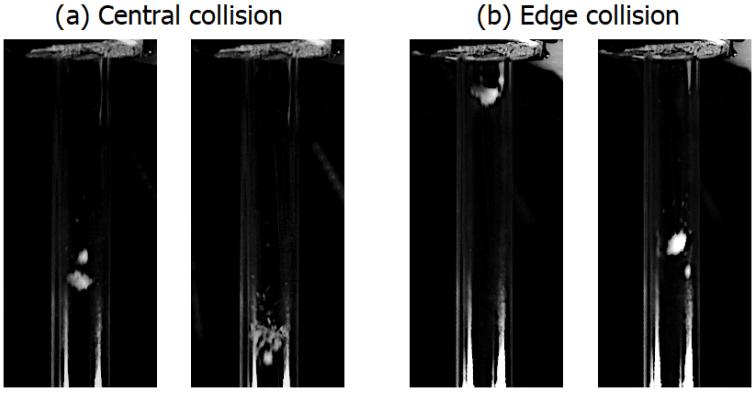

Figure 10. Two types of graupel-snowflake collision above the HIVIS instrument inside the cold room with (a) central collision and (b) edge collision. The left picture represents the two particles before and right picture after the collision for (a) and (b).

As snowflakes were formed under still air conditions, some crystals monomers or crystal branches were expelled because of the increasing of drag forces during the fall. To characterize this artificial enhancement of ice crystal fragment number in the results, five snowflakes were launched into the tube without collision. This blank measurement resulted in 26 to 140 fragments, with a mean of 51 fragments. This number of fragments was subtracted from the total number of crystals produced by collisions. It should also be noticed that these collisions were carried out in undersaturated conditions around 90% ice saturation. Although sublimation can potentially cause dendritic structures to weaken, resulting in an increased production of fragments compared to saturated conditions, this effect was likely limited in this experiment. This is because the snowflake spent less than 30 seconds in the air under these conditions before falling, and the fall of both the snowflake and its fragments lasted only about 1 second. As a result, any sublimation-induced weakening effect on the size and number of fragments observed was likely minimal.

3.2.2 Hologram reconstruction and fragment tracking

Crystal images were reconstructed from holograms (see details in Weitzel et al., 2020) at each Δz=100 µm distance along the optical axis (see Fig. 9) using the method of Fugal et al. (2004). The particle properties were determined in terms of the major

https://doi.org/10.5194/egusphere-2023-1074
Preprint. Discussion started: 6 June 2023

and minor axis. Furthermore, the cross section area was obtained from a particle detection algorithm of Fugal et al. (2009). To distinguish ice fragments and artifacts (i.e. holograms resulting from noise, optics imperfection and reconstruction method), a decision tree based on the particle properties was created and applied to the reconstructed objects for each collision.

As fragments are falling slowly through the sampling volume, the same crystal can be seen on successive holographic images. To avoid counting crystals several times and to identify the repetition of the same fragments between frames, a tracking program was developed. The tracking was based on predicted position of the fragments at the subsequent time step from an initial fragment position. This prediction is based on the fall speed parametrization $v_T = 0.67{D_{max}}^{0.46}$ (Vázquez-Martín et al., 2021) valid for spatial stellar ice crystals. All fragments present in the area of an ellipse surrounding the predicted position were selected as being the potentially preceding crystal. During the analysis, the ellipse size was manually adjusted to 6 mm major axis and 1.2 mm minor axis to be able to track all crystals. The size of the ellipse was chosen after several tests to follow the large millimeter sized crystals while avoiding counting other nearby crystals. The dimensions (maximum size,cross-sectional area, and aspect ratio) of all fragments found in the designated area were compared to those of the initial crystal. If one of these dimensions varied by more than 30% from the preceding particle, the fragment was not considered the initial one. After multiple comparisons with a visual track of the fragments, this deviation was deemed appropriate and provides the best balance for identifying the correct fragments. This condition is especially useful when multiple fragments are present in the ellipse area and helps select a crystal that matches the characteristics. The program was also tested using deviation values of 20% and 60% to determine the error in the total number of fragments produced (see error bars in Fig. 14), accounting for factors such as rotation of the fragments.

4 Results and discussion

4.1 Graupel-graupel collisions

The measured number of fragments produced by graupel-graupel collisions from our experiments as a function of the CKE is shown in Fig. 11. Apparently, the number fragments increases exponentially with the CKE which was expected regarding Takahashi et al. (1995). A power law fit of this dependency on our data gives

$$N = 5.14 \times 10^4 \times CKE^{0.41} \tag{3}$$

with N being the number of fragments produced (CKE in J). It is expected that a maximum of ice fragments is reached at a certain CKE (Phillips et al., 2017). Such a maximum is not observed here within the investigated CKE range between 10^{-7} J and $2{\times}10^{-5}$ J. This power law can therefore be considered as valid only for the measured CKEs. Using the parameterization of Phillips et al. (2017) which is based on the data of Takahashi et al. (1995), a fragment number of less than 20 would be predicted, i.e. much less than in our measurements. Or, stated differently, a higher CKE between 5×10^{-4} J and 5×10^{-3} J is required in Phillips et al. (2017) to generate a fragment number between 200 and 450 for hail-hail collisions. Considering the intermediate CKE which represents typical collision conditions in natural clouds (Takahashi, 1993), an average of 310 fragments was ejected during collisions. This is in contrast to Takahashi et al. (1995) who estimated 60 fragments from their

https://doi.org/10.5194/egusphere-2023-1074
Preprint. Discussion started: 6 June 2023

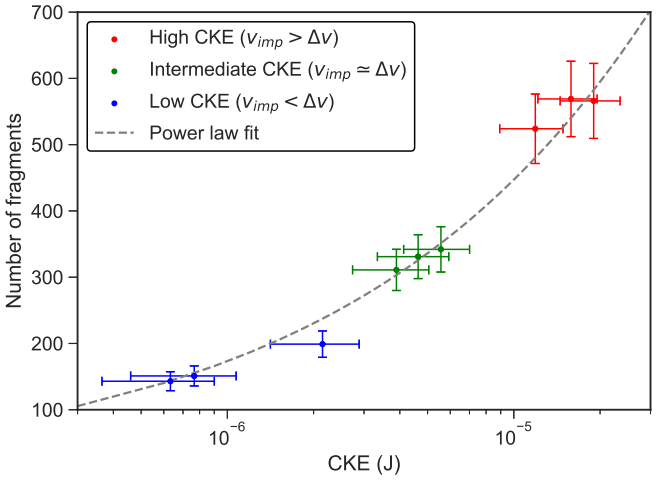

Figure 11. Number of fragments produced by graupel-graupel collisions as a function of the CKE. Low CKE in blue, intermediate in green, and high in red (see section 3.1.2)

experiments. This difference could be due to the use of two 1.8 cm rigidly fixed ice spheres instead of millimeter-size flexible mounted rimed graupel, as in our experiments. As illustrated in Fig. 2, the pure ice structure reduces vapor growth of ice crystals compared to a rimed graupel surface. Furthermore, Takahashi et al. (1995) experiments did not take into account the ventilation effect of a falling graupel, which can, due to its cooling effect, increase the growth rate of the crystals. These two possible effects imply that the Takahashi et al. (1995) experiments very likely lead to a slow crystal growth, which can of course induce a reduction of the number of fragments as the fragility of ice crystals increases with their size (Phillips et al., 2017). We also observed that for longer vapor deposition growth times, the number of fragments increases similarly to the finding in Takahashi et al. (1995). Up to 800 fragments were produced by graupel-graupel collisions in our study for 20 minutes growth time, which is close to the maximum number of crystals observed at -15°C in Takahashi et al. (1995). The mean number of the crystals growing on the graupel surface was estimated to be around 38 $\pm$ 13 from microscope images (see Fig. 5). This number is probably underestimated since crystals smaller than 100 µm were not identifiable on the graupel surface. The average size distribution of these crystals is represented in Fig. 12 by a black dotted line. First test results revealed also, that the number of fragments produced in bare (i.e. withouth dendritic crystals on the surface) graupel-graupel collisions was negligible. This supports the study of Griggs and Choularton (1986) where a pure rime structure was inefficient to produce ice fragments.

For each of the collisions, a fragment size distribution (FSD) was calculated from the analysis of the ice crystal images. The average FSDs for the three CKE ranges are presented in Fig. 12. The FDs obtained from the single experiments can be found in Appendix B1.

https://doi.org/10.5194/egusphere-2023-1074
Preprint. Discussion started: 6 June 2023

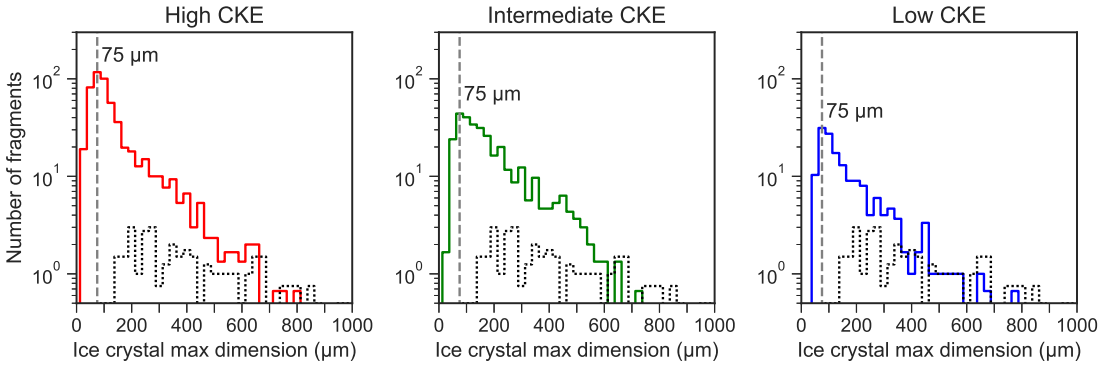

Figure 12. Average fragment size distributions as solid line for different CKE ranges of graupel-graupel collisions: blue: low; green: intermediate; and red: high CKE. Average size distribution of crystals on graupel surface as black dotted line.

As obvious from Fig. 12, the FSDs have similar shapes, all having a maximum of fragment number around 75 µm. This result is in agreement with Takahashi (1993) in-situ observation of 60 and 100 µm crystals at -15 °C and -20 °C, respectively, when both large and small graupel were present. Our laboratory study supports therefore Takahashi's hypothesis, who suggested that the observed airborne ice crystals were produced by graupel-graupel collisions. A general parametrization of the FSD for all CKEs is given in Fig. 13.

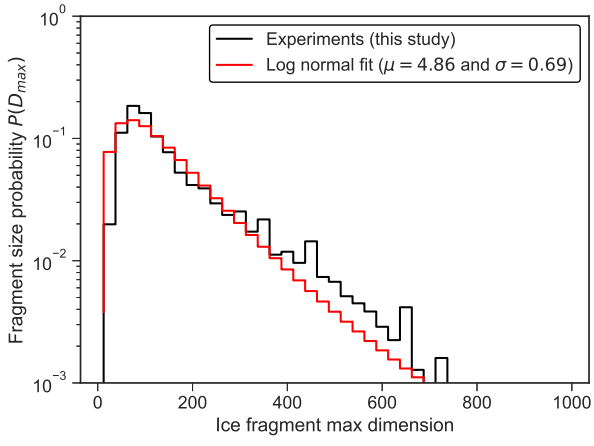

Figure 13. Parametrization for fragment size distribution from our collision experiments. Integrated log-normal probability density function in red and initial data from experiments in black.

https://doi.org/10.5194/egusphere-2023-1074
Preprint. Discussion started: 6 June 2023

Similarly to drop-drop collisions of Low and List (1982), a log-normal probability density function is used to fit the collision experiments:

$$f(D) = \frac{1}{\sigma D\sqrt{2\pi}} e^{\frac{(\ln(D)-\mu)^2}{2\sigma^2}} \quad (4)$$

with D the fragment maximum dimension, μ the position parameter and σ the shape parameter. The two parameters μ=4.86 and σ=0.69 are obtained from all collisions experiments, considering 3136 fragments. These values can be considered as valid for our CKE range at -15 °C. In case of discrete bins, such as in Fig. 13, a simple multiplication with the bin width is necessary to get the crystal size probability with $P(D_i) = f(Di)\Delta Di$. A higher kinetic energy increases slightly the probability to get small fragments (see Fig. 12). However, this effect is restricted to small crystals around 25 µm and remains negligible for the FSD parametrization.

Area and aspect ratio distributions of the fragments were also obtained from the microscope images and are presented in Fig. C1 and Fig. D1. The shape of the area size distributions seems to be independent of the CKE. However, the minimal surface area of the fragments is located around 2×10^{-4} mm^2 for high CKE, while it is 5×10^{-4} mm^2 for intermediate and low CKE. This decrease of the minimum fragment area can be explained by the fact that the work done to break crystals is proportional to their cross-sectional area (Phillips et al., 2017). This consideration also applies to the observed higher frequency of 25 µm crystals as the CKE increases (see Fig. 12). However, this observation should be taken with caution because the limit of detection of ice fragments with the microscope is estimated to be around 20 µm for crystal maximum dimension and around 10^{-4} mm^2 for crystal area. Figure D1 depicts the aspect ratio of the ice fragments, which is calculated as the ratio between the minor and the major length (AR=D_{min}/D_{maj}) of the ellipse fitted on the fragments edges. More than 90% of the crystals have an AR higher than 0.4, and crystals with an AR around 0.7 are the most frequent.

4.2 Graupel-snowflake collisions

Figure 14 shows the number of fragments produced by graupel-snowflake collisions as a function of the CKE for different impact position parameters. Two distinct cases of collisions were observed: (i) the graupel impacts the center of the snowflake which is therefore completely broken (Fig. 10a); and (ii) the graupel hits the edge of the snowflake breaking some crystals and producing a rotation of the entire snowflake (Fig. 10b). It is apparent from Fig. 14 that the position where the graupel hits the snowflake, influences the number of produced fragments. Less than 200 fragments are generated for I_p close to 0 while more than 200 fragments are produced for I_p close to 1. Collisions with intermediate impact parameters are represented in green/light blue in Fig. 14.

The number of fragments produced by graupel-snowflake collisions is increasing from around 50 to more than 400 depending on the CKE. In Fig. 14, the errors in the number of fragments are calculated as described in section 3.2.2. The graupel-graupel fit from Fig. 11 is plotted as a dashed line in Fig. 14, which fits also well on the data points of the graupel-snowflake collisions, indicating that the two types of collisions are similar in terms of CKE dependency and produced number of fragments. Data

https://doi.org/10.5194/egusphere-2023-1074
Preprint. Discussion started: 6 June 2023

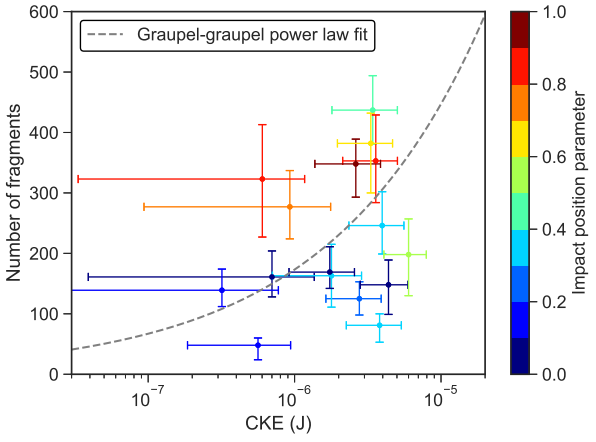

Figure 14. Number of fragments produced by graupel-snowflake collisions as a function of the CKE and impact position parameter I_p represented in a color scale from blue to red.

points corresponding to the central position of the graupel-snowflake collisions are lying slightly above the graupel-graupel fit, while those of edge collisions are lying below. It remained an open question after our collision experiments, whether the observed dependence of the number of fragments on the CKE is generally valid for all particles with dendritic crystals.

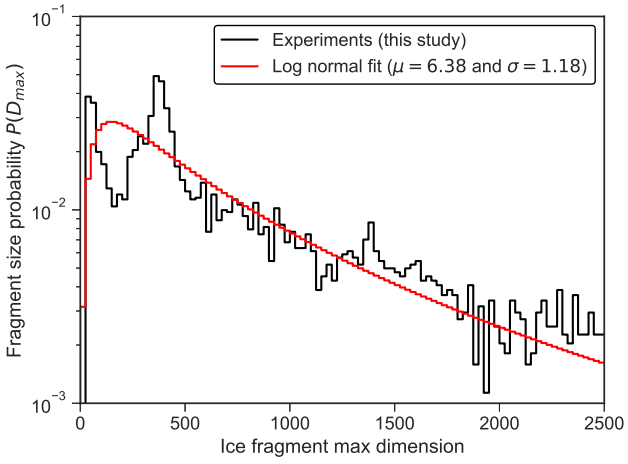

Figure 15. Mean fragment size distribution from all graupel-snowflake collision experiments. Integrated log-normal probability density function in red and initial data from experiments in black.

350 In Fig. 15 the mean fragment size distribution is represented from 16 single graupel-snowflake collisions (see Appendix B2). The majority of fragments are distributed between 0 and 2000 µm with two modes observed around 50 µm and 400 µm. The

https://doi.org/10.5194/egusphere-2023-1074
Preprint. Discussion started: 6 June 2023

observed millimeter-size fragments are probably single crystals that are ejected from the snowflake structure during collision while hundred-micrometer fragments might originate from the breakup of single crystals by the collision with the graupel.

Two modes can be identified in the mean FSD of Fig. 15 which is different to the unimodal FSD observed for graupel-graupel collisions in Fig. 13. However, as shown in Appendix B2, these two modes are not systematically present in single collision experiments, in which only half of the collisions resulted in two modes. The presence of these two peaks does not seem to be related to the impact position or to the CKE. It is very likely that the manual production of snowflakes generates diverse ice structures for the different snowflakes that can lead to distinct fragment sizes, and therefore, to the presence of a second mode around 50 µm for some collisions. A lognormal distribution was fitted to the mean particle size distribution (Fig. 15) from Eq. 4 as for the graupel-graupel FSD. This fit with the two parameters $\mu = 6.38$ and $\sigma = 1.18$ can be used to represent the general trend of the distribution but remains imprecise in representing the two modes.

Vardiman (1978) carried out ice particle collision experiments with rimed dendrites and graupel. From experimental results and with a model based on change of momentum between the incoming ice particles, he described the time evolution of size distribution from several graupel-rimed-dendrite collisions. The graupel collisions with rimed dendrites (both particles are around 1 mm in diameter) can be comparable to our graupel-snowflake collision as our snowflakes were generated using dendritic crystals. The size of fragments resulting from dendrites are distributed between 0 and 2500 µm, with a mode between 300 and 500 µm which is close to our observations for unimodal distributions for graupel-snowflake collisions. However, no second mode near 50 µm similar to the one observed during our experiments was reported by Vardiman (1978).

For graupel-snowflake collisions the fragment areas are distributed between 5×10^{-3} and 10^2 mm^2 (see Appendix C2). It can be noticed that the smallest fragment area of these distribution and the shape of the distributions are close to those of graupel-graupel collisions. As can be seen in Appendix D2, the aspect ratio of the fragments in graupel-snowflake collisions is slightly lower than that of graupel-graupel collisions, with a maximum of fragments emitted at AR=0.5.

5 Conclusions

Two new experimental setups were designed and implemented in the cold room of the Johannes Gutenberg University of Mainz, Germany, to obtain the number, size and shape of fragments resulting from atmospheric ice particle collisions around -15°C. First, the collision of two graupel particles was studied. In these experiments, a graupel particle with a diameter of 4 mm was released to fall onto another graupel particle with a diameter of 2 mm. The second particle was mounted on a thin wire, enabling it to move following the collision.All fragments generated during the collisions were collected and investigated under a microscope. The results of these graupel-graupel collisions revealed that the number of fragment (150 to 550) is exponentially increasing with the collision kinetic energy (CKE). This evolution and the number of fragments are similar to the findings of Takahashi et al. (1995). However, a significantly higher CKE is required in Takahashi et al. (1995) or Phillips et al. (2017) to obtain the same number of particles as in our study. A large number of fragments have a maximum dimension of around 75 µm which is consistent with the 60 to 100 µm ice crystals observed in Takahashi (1993). The number of the smallest fragments

https://doi.org/10.5194/egusphere-2023-1074
Preprint. Discussion started: 6 June 2023

(25 μm) seems to be the only parameter which depends on the CKE. A parameterization of the size of the fragments produced by graupel-graupel collisions is therefore made for all measurements including all CKEs.

Several non-realistic aspects of Takahashi et al. (1995) experiments such as the size of ice particles and riming in still air were pointed out in Korolev and Leisner (2020). These aspects have been considered in our experiments by generating more realistic sizes of graupel particles, and by using an updraft during the riming and dendritic growth processes. It should be noted that keeping the small graupel in position with a fibre creates aerodynamic resistance which can increase the number of generated fragments. However, it is difficult to produce free-fall collisions at the terminal fall speeds of these particles because of their high terminal velocities. Keeping the graupel on a thin wire seems to be the best way to control this experiment while letting the particles freely move after collision.

In the second series of experiments the collisions of a graupel and a dendritic ice crystal aggregate as proxy for a snowflake were studied. These collisions were investigated as both particles were freely falling inside a fall tube. All fragments resulting from the collisions were recorded by a holographic imaging instrument. The results show that the number of produced fragments is between 50 and 450, depending on the CKE and the position where the graupel hits the snowflake. In accordance to the fragment size distribution of Vardiman (1978), we also found one mode of the FSD at 400 µm but a second one at 50 µm for half of collisions. The results obtained here show that the number of fragments produced is certainly underestimated regarding the coefficients provided by Phillips et al. (2017) parameterization for our CKE range.

This study is a step towards a better understanding of the fragmentation breakup of ice crystals in collisions where at least one particle have dendritic (i.e. fragile) ice crystal on its surface. Our results highlight the necessity for further investigation of collision induced fragment production of atmospheric ice particles, and the dependence of the process on temperature, rimed fraction, particle size and type, and dendritic growth time. By means of improved experimental designs it might even become possible to use natural snow flakes after capturing these in the open atmosphere.

Data availability. The data set used for generating the figures is available under https://doi.org/10.5281/zenodo.7877368. The raw measurement data will be provided upon request.

Video supplement. A video supplement showing the records of the graupel-graupel, graupel-snowflake (edge), and graupel-snpwflake (central) collisions can be downloaded from https://doi.org/10.5446/62064, https://doi.org/10.5446/62065, and https://doi.org/10.5446/62066, respectively.

https://doi.org/10.5194/egusphere-2023-1074
Preprint. Discussion started: 6 June 2023

Appendix A: Graupel free fall equations

The equation of motion for a spherical liquid drop from Pruppacher and Klett (2010) can be used to describe the motion of a lump graupel which is almost spherical with

$$m_g \frac{dv}{dt} = (m_g + m_a)g - \frac{1}{2}\rho_a C_d A v^2 = \left(1 - \frac{\rho_a}{\rho_g}\right)g - \frac{3}{8}\frac{C_d \rho_a}{\rho_g r}v^2. \tag{A1}$$

where m_g and m_a the graupel and air masses, ρ_g and ρ_a are the graupel and air densities, g the acceleration, A the graupel cross section, C_d the drag coefficient, r the radius of the graupel and v the graupel fall speed. The previous equation can be simplified with C_1 and C_2 terms:

$$\frac{dv}{dt} = C_1 - C_2 v^2. \tag{A2}$$

Equation A2 have to be integrated to deduce the speed and the position of the graupel during the fall speed as

$$t = \int \frac{1}{C_1 - C_2 v^2} dv = \int \frac{1}{(\sqrt{C_1} - \sqrt{C_2}v)(\sqrt{C_1} + \sqrt{C_2}v)} dv \tag{A3}$$

$$t = \int \frac{1}{2\sqrt{C_1}(\sqrt{C_1} + \sqrt{C_2}v)} + \frac{1}{2\sqrt{C_1}(\sqrt{C_1} - \sqrt{C_2}v)} dv \tag{A4}$$

$$t = \frac{1}{2\sqrt{C_1}}\left(\frac{\ln(\sqrt{C_1} + \sqrt{C_2}v)}{\sqrt{C_2}} - \frac{\ln(\sqrt{C_1} - \sqrt{C_2}v)}{\sqrt{C_2}}\right) = \frac{1}{2\sqrt{C_1 C_2}} \ln\left(\frac{1 + \sqrt{C_2}/\sqrt{C_1}v}{1 - \sqrt{C_2}/\sqrt{C_1}v}\right). \tag{A5}$$

From Eq. A5 and the $\mathrm{arctanh}$ function properties

$$t = \frac{1}{\sqrt{C_1 C_2}} \mathrm{arctanh}\left(\frac{\sqrt{C_2}}{\sqrt{C_1}}v\right). \tag{A6}$$

By integrating Eq. A6, one can deduce the speed of the graupel depending on the time

$$v = \frac{\sqrt{C_1}}{\sqrt{C_2}} \tanh\left(\sqrt{C_1}\sqrt{C_2}t\right). \tag{A7}$$

To know the position of the graupel according to the time, equation A7 have to be integrated. With the properties of the $\tanh$ function, the position of the graupel is expressed by

$$x = \frac{1}{\sqrt{C_1}} \ln\left(\cosh\left(\sqrt{C_1 C_2}t\right)\right). \tag{A8}$$

If $t \to \infty$, the fall velocity becomes equal to the terminal velocity v_T of the graupel:

$$v_T = \sqrt{\frac{8r(\rho_a/\rho_g - 1)g}{3C_d}}. \tag{A9}$$

https://doi.org/10.5194/egusphere-2023-1074
Preprint. Discussion started: 6 June 2023

Appendix B: Fragments size distributions of graupel-graupel collisions

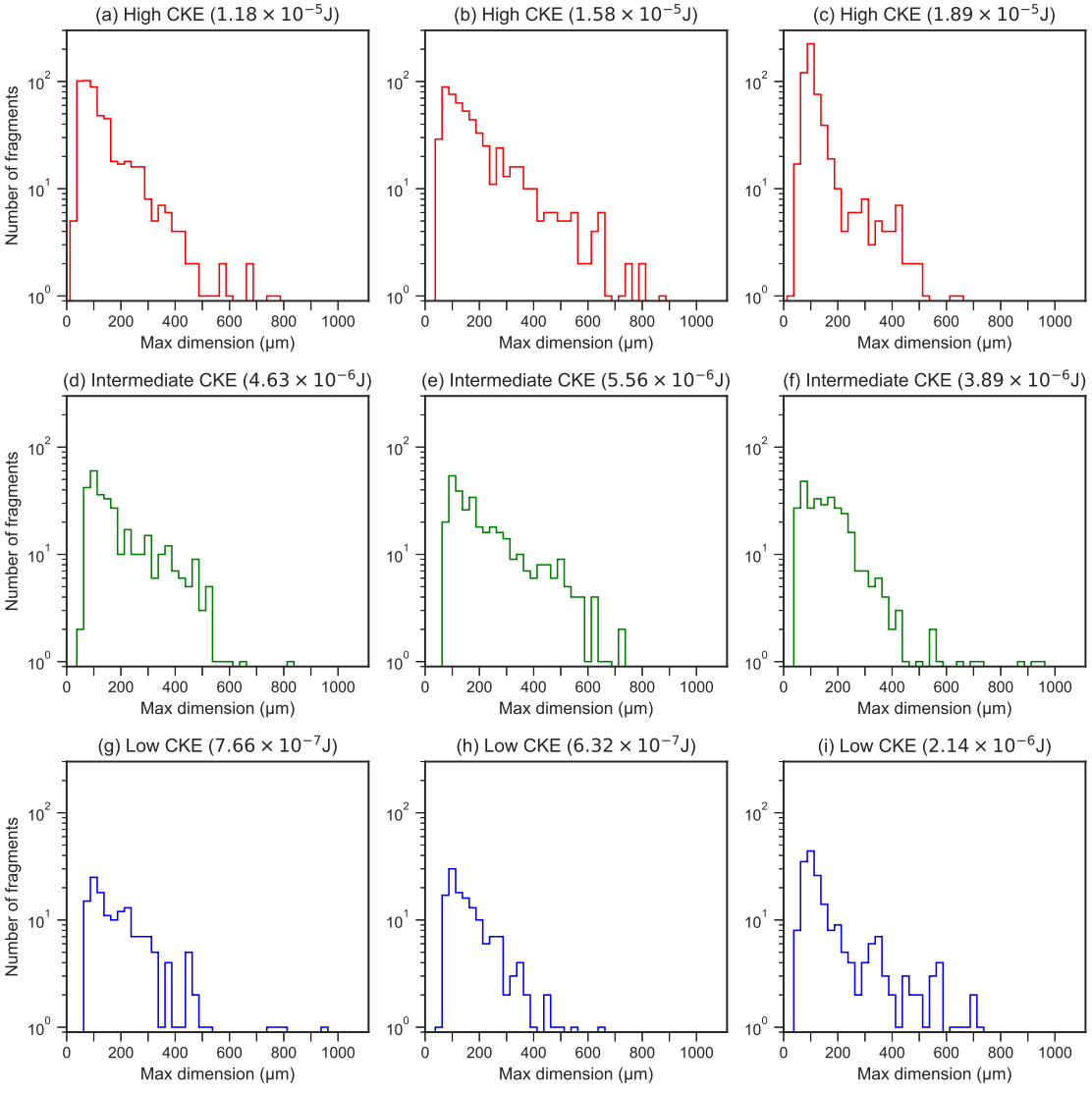

Figure B1. Size distributions of ice fragments produced by graupel-graupel collisions. Low CKE in blue, intermediate CKE and high CKE in red.

https://doi.org/10.5194/egusphere-2023-1074
Preprint. Discussion started: 6 June 2023

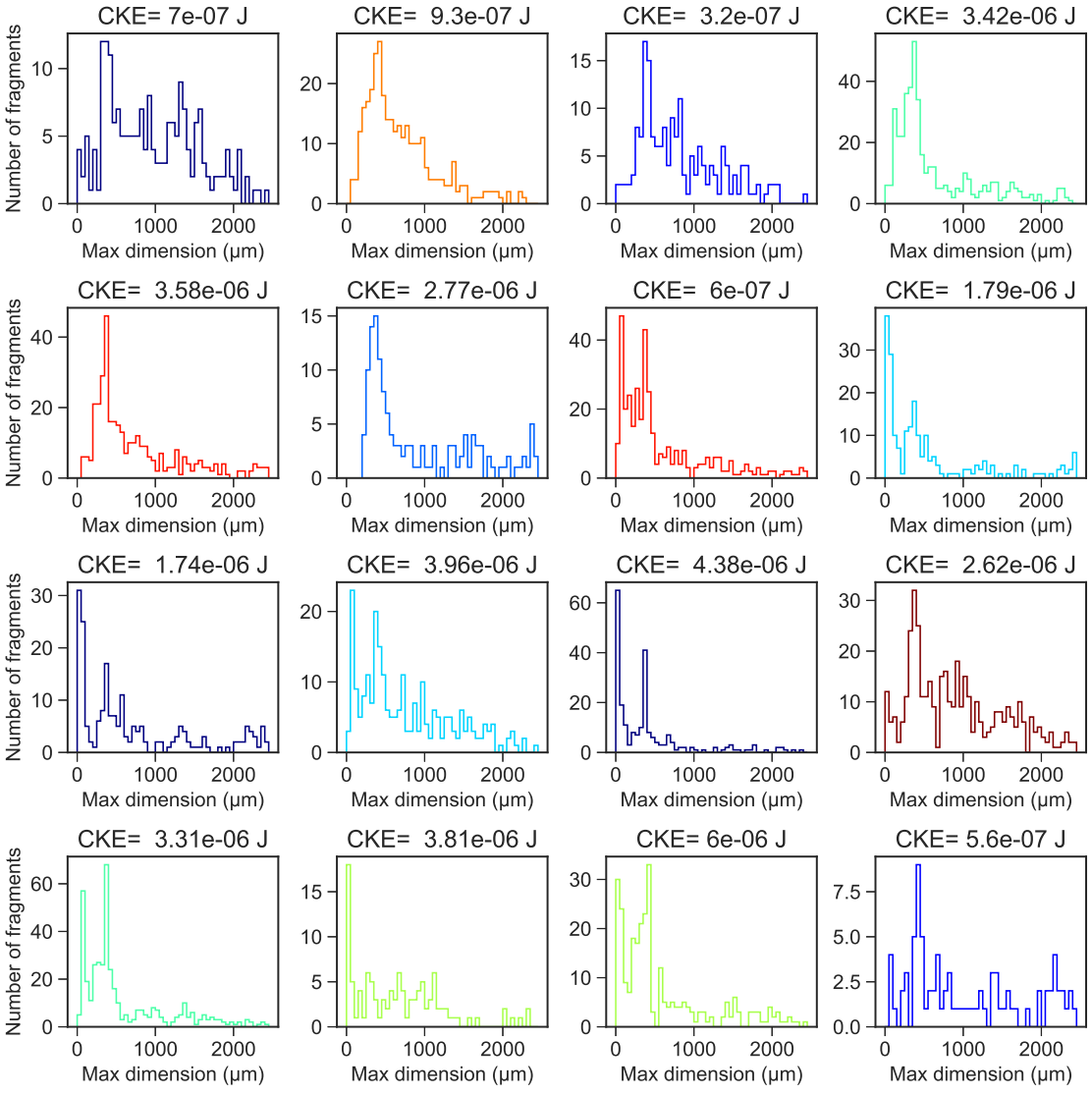

Figure B2. Size distributions of ice fragments produced by graupel-snowflake collisions for different impact positions (see color scale of Fig. 14).

https://doi.org/10.5194/egusphere-2023-1074
Preprint. Discussion started: 6 June 2023

Appendix C: Distributions for the cross sectional areas of the fragments

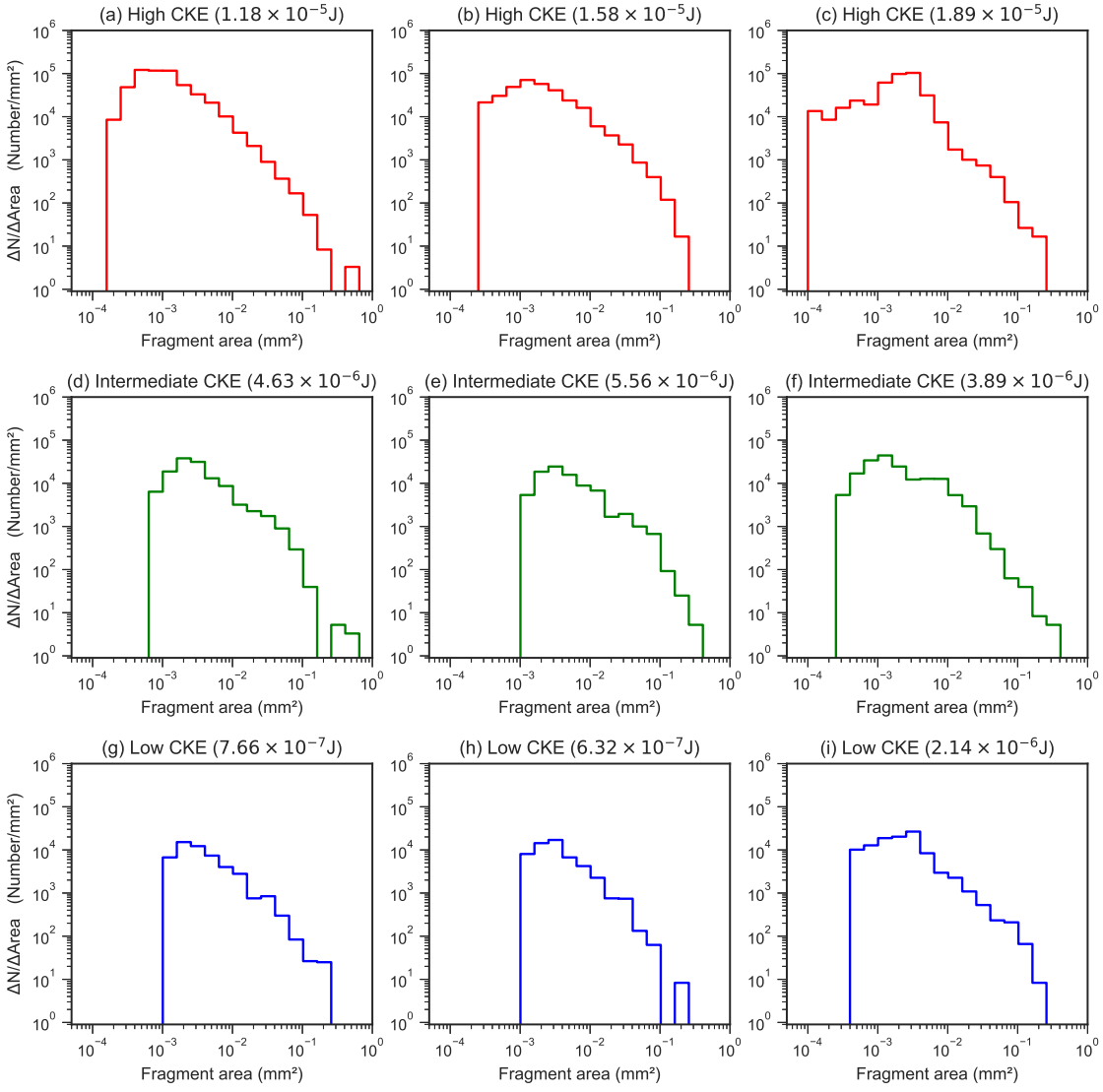

Figure C1. Area distributions of ice fragments produced by graupel-graupel collisions. Low CKE in blue, intermediate CKE and high CKE in red.

https://doi.org/10.5194/egusphere-2023-1074
Preprint. Discussion started: 6 June 2023

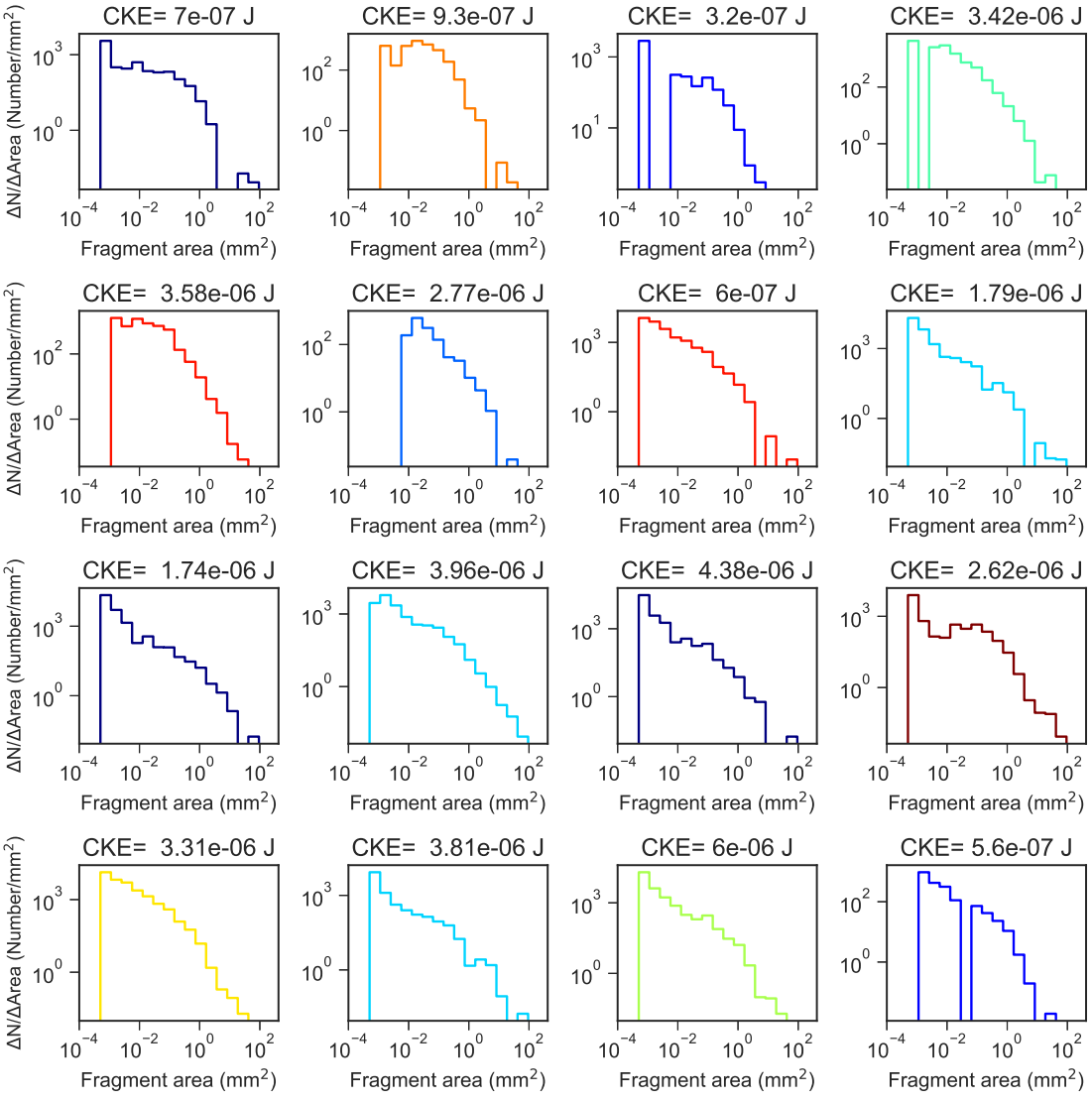

Figure C2. Area distributions of ice fragments produced by graupel-snowflake collisions for different impact positions (see color scale of Fig. 14).

https://doi.org/10.5194/egusphere-2023-1074
Preprint. Discussion started: 6 June 2023

Appendix D: Distributions of fragments aspect ratio

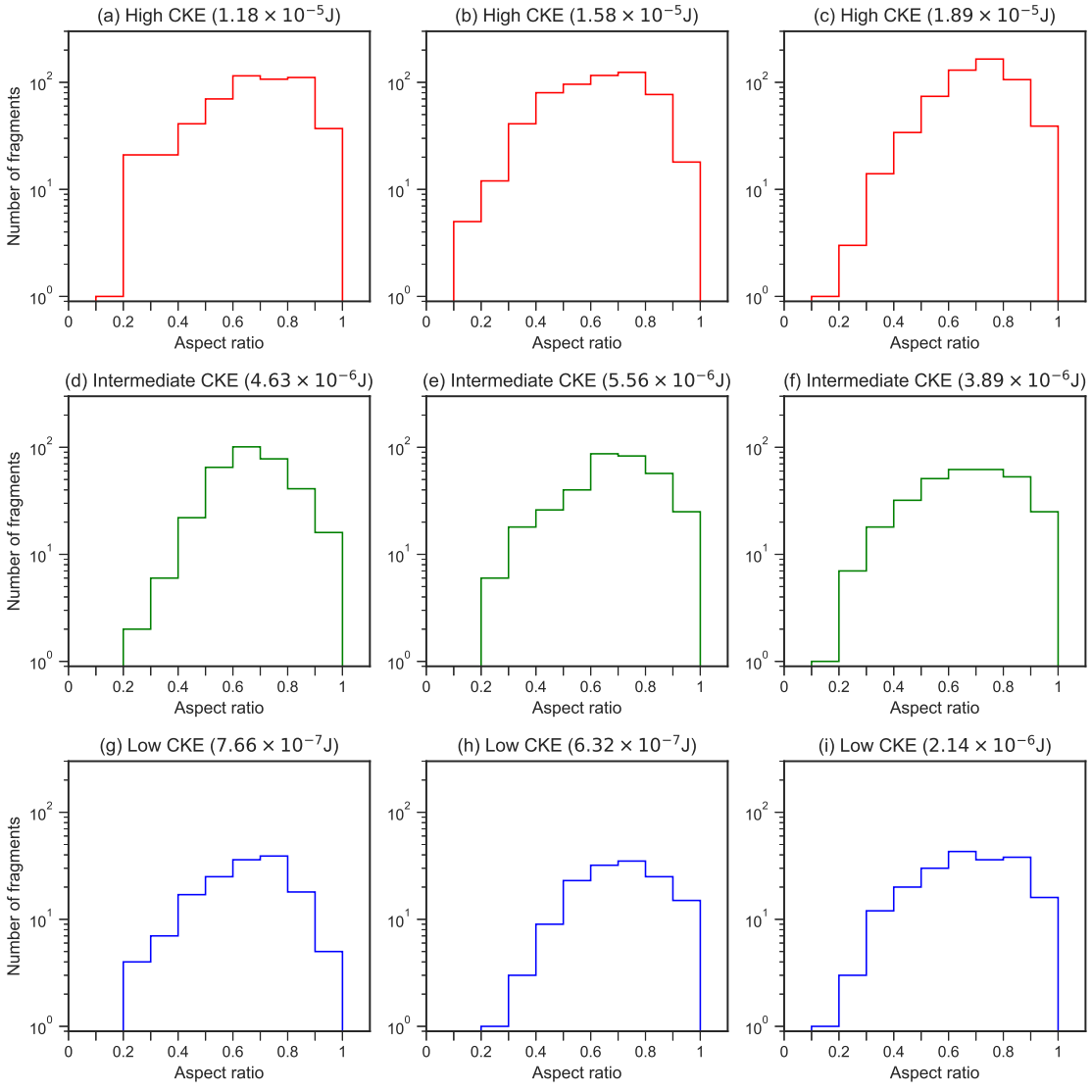

Figure D1. Aspect ratio (AR=D_{min}/D_{maj}) distributions of ice fragments produced by graupel-graupel collisions. Low CKE in blue, intermediate CKE and high CKE in red.

https://doi.org/10.5194/egusphere-2023-1074
Preprint. Discussion started: 6 June 2023

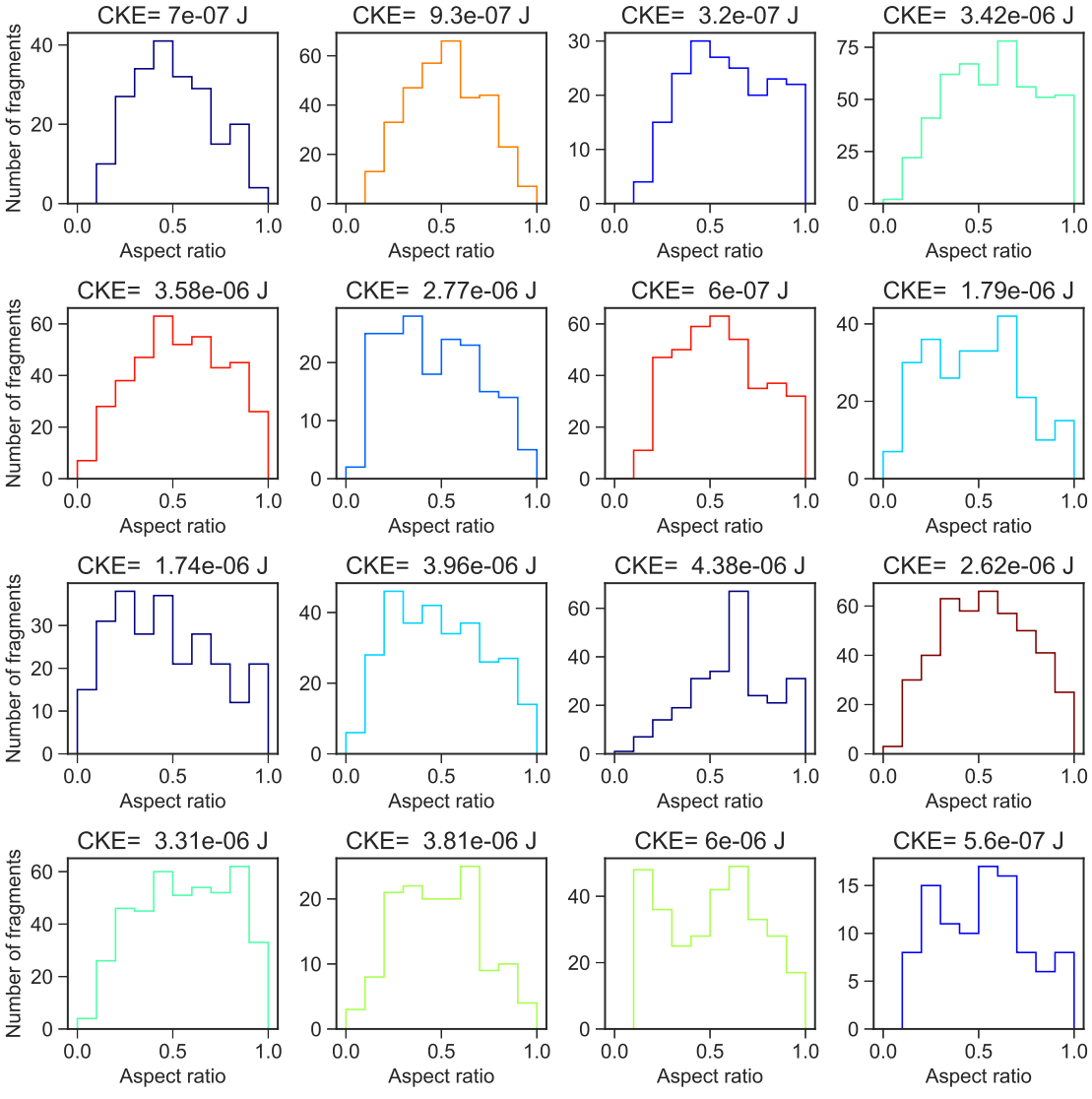

Figure D2. Aspect ratio (AR=D_{min}/D_{maj}) distributions of ice fragments produced by graupel-snowflake collisions for different impact positions (see color scale of Fig. 14).

Author contributions. The paper was written by P.G. and M.S. with the support and assistance of all co-authors; SB, made significant contributions by providing comments on the results, discussion, and conclusion; P.G. and F.Z. performed graupel growth experiments; P.G. carried out collision experiments, and evaluated the data; S.Y. performed ice crystal growth experiments and analyzed the data; F.Z. evaluated and analyzed the holographic data; A.T. constructed the graupel generator, designed the graupel growth and dendritic crystal growth

https://doi.org/10.5194/egusphere-2023-1074
Preprint. Discussion started: 6 June 2023

experiments, and holographic measurements; S.K.M. and P.G. designed the graupel growth, crystal growth and collision experiments; M.S. designed the experiments, analyzed the data.

Competing interests. The authors declare no competing interest.

Acknowledgements. We gratefully acknowledge the funding of the German Research Foundation (DFG) to initialize the special priority programme on the Fusion of Radar Polarimetry and Atmospheric Modelling (SPP-2115, PROM). The work of contributing authors was carried out in the framework of the project "FRAGILE: Exploring the role of FRAGmentation of ice particles by combining super-partIcle modelling, Laborotary studies, and polarimEtric radar observations" (Grant KN 1112/5). We also gratefully acknowledge funds from internal Max Planck Institute for Chemistry (Mainz, Germany) budget. Figures 1, 2, 6, and 9a have been created with BioRender.com.

https://doi.org/10.5194/egusphere-2023-1074
Preprint. Discussion started: 6 June 2023

References

Field, P. R. and Heymsfield, A. J.: Importance of snow to global precipitation, Geophysical Research Letters, 42, 9512–9520, https://doi.org/10.1002/2015gl065497, 2015.

Field, P. R., Lawson, R. P., Brown, P. R. A., Lloyd, G., Westbrook, C., Moisseev, D., Miltenberger, A., Nenes, A., Blyth, A., Choularton, T., Connolly, P., Buehl, J., Crosier, J., Cui, Z., Dearden, C., DeMott, P., Flossmann, A., Heymsfield, A., Huang, Y., Kalesse, H., Kanji, Z. A., Korolev, A., Kirchgaessner, A., Lasher-Trapp, S., Leisner, T., McFarquhar, G., Phillips, V., Stith, J., and Sullivan, S.: Chapter 7. Secondary Ice Production - current state of the science and recommendations for the future, Meteorological Monographs, https://doi.org/10.1175/amsmonographs-d-16-0014.1, 2017.

Flossmann, A. I. and Wobrock, W.: A review of our understanding of the aerosol–cloud interaction from the perspective of a bin resolved cloud scale modelling, Atmospheric Research, 97, 478–497, https://doi.org/https://doi.org/10.1016/j.atmosres.2010.05.008, from the Lab to Models and Global Observations: Hans R. Pruppacher and Cloud Physics, 2010.

Fries, E., Haunold, W., Jaeschke, W., Hoog, I., Mitra, S. K., and Borrmann, S.: Uptake of gaseous aromatic hydrocarbons by non-growing ice crystals, Atmospheric Environment, 40, 5476–5485, https://doi.org/https://doi.org/10.1016/j.atmosenv.2006.03.055, 2006.

Fugal, J. P., Shaw, R. A., Saw, E. W., and Sergeyev, A. V.: Airborne digital holographic system for cloud particle measurements, Appl. Opt., 43, 5987–5995, https://doi.org/10.1364/AO.43.005987, 2004.

Fugal, J. P., Schulz, T. J., and Shaw, R. A.: Practical methods for automated reconstruction and characterization of particles in digital in-line holograms, Measurement Science and Technology, 20, 075 501, https://doi.org/10.1088/0957-0233/20/7/075501, 2009.

Griggs, D. J. and Choularton, T. W.: A laboratory study of secondary ice particle production by the fragmentation of rime and vapour-grown ice crystals, Quarterly Journal of the Royal Meteorological Society, 112, 149–163, https://doi.org/10.1002/qj.49711247109, 1986.

Hallett, J., Sax, R. I., Lamb, D., and Murty, A. S. R.: Aircraft measurements of ice in Florida cumuli, Quarterly Journal of the Royal Meteorological Society, 104, 631–651, https://doi.org/10.1002/qj.49710444108, 1978.

Heymsfield, A. and Wright, R.: Graupel and Hail Terminal Velocities: Does a "Supercritical" Reynolds Number Apply?, Journal of the Atmospheric Sciences, 71, 3392–3403, https://doi.org/10.1175/jas-d-14-0034.1, 2014.

Heymsfield, A., Szakáll, M., Jost, A., Giammanco, I., and Wright, R.: A Comprehensive Observational Study of Graupel and Hail Terminal Velocity, Mass Flux, and Kinetic Energy, Journal of the Atmospheric Sciences, 75, 3861–3885, https://doi.org/10.1175/jas-d-18-0035.1, 2018.

Heymsfield, A. J., Schmitt, C., Chen, C.-C.-J., Bansemer, A., Gettelman, A., Field, P. R., and Liu, C.: Contributions of the Liquid and Ice Phases to Global Surface Precipitation: Observations and Global Climate Modeling, Journal of the Atmospheric Sciences, 77, 2629–2648, https://doi.org/10.1175/jas-d-19-0352.1, 2020.

Hobbs, P. V. and Farber, R.: Types of snowfall, Journal de Recherches Atmosphériques, 6, 245–258, 1972.

Hobbs, P. V., Politovich, M. K., and Radke, L. F.: The Structures of Summer Convective Clouds in Eastern Montana. I: Natural Clouds, Journal of Applied Meteorology, 19, 645–663, https://doi.org/10.1175/1520-0450(1980)019<0645:tsoscc>2.0.co;2, 1980.

Huang, Y., Wu, W., McFarquhar, G. M., Xue, M., Morrison, H., Milbrandt, J., Korolev, A. V., Hu, Y., Qu, Z., Wolde, M., Nguyen, C., Schwarzenboeck, A., and Heckman, I.: Microphysical processes producing high ice water contents (HIWCs) in tropical convective clouds during the HAIC-HIWC field campaign: dominant role of secondary ice production, Atmospheric Chemistry and Physics, 22, 2365–2384, https://doi.org/10.5194/acp-22-2365-2022, 2022.

Jiusto, J. E. and Weickmann, H.: Types of snowfall, Bulletin of the American Meteorological Society, 54, 1148–1162, 1973.

https://doi.org/10.5194/egusphere-2023-1074
Preprint. Discussion started: 6 June 2023

Karalis, M., Sotiropoulou, G., Abel, S. J., Bossioli, E., Georgakaki, P., Methymaki, G., Nenes, A., and Tombrou, M.: Effects of secondary ice processes on a stratocumulus to cumulus transition during a cold-air outbreak, Atmospheric Research, 277, 106 302, https://doi.org/10.1016/j.atmosres.2022.106302, 2022.

Kikuchi, K., Kameda, T., Higuchi, K., and Yamashita, A.: A global classification of snow crystals, ice crystals, and solid precipitation based on observations from middle latitudes to polar regions, Atmospheric Research, 132-133, 460–472, https://doi.org/https://doi.org/10.1016/j.atmosres.2013.06.006, 2013.

Kobayashi, T.: The growth of snow crystals at low supersaturations, Philosophical Magazine, 6, 1363–1370, https://doi.org/10.1080/14786436108241231, 1961.

Korolev, A. and Leisner, T.: Review of experimental studies of secondary ice production, Atmospheric Chemistry and Physics, 20, 11 767–11 797, https://doi.org/10.5194/acp-20-11767-2020, 2020.

Korolev, A., DeMott, P. J., Heckman, I., Wolde, M., Williams, E., Smalley, D. J., and Donovan, M. F.: Observation of secondary ice production in clouds at low temperatures, Atmospheric Chemistry and Physics, 22, 13 103–13 113, https://doi.org/10.5194/acp-22-13103-2022, 2022.

Low, T. B. and List, R.: Collision, Coalescence and Breakup of Raindrops. Part II: Parameterization of Fragment Size Distributions, Journal of the Atmospheric Sciences, 39, 1607–1619, https://doi.org/10.1175/1520-0469(1982)039<1607:ccabor>2.0.co;2, 1982.

Mossop, S.: The origin and concentration of ice crystals in clouds, Bulletin of the American Meteorological Society, 66, 264–273, 1985.

Phillips, V. T. J., Yano, J.-I., and Khain, A.: Ice Multiplication by Breakup in Ice–Ice Collisions. Part I: Theoretical Formulation, Journal of the Atmospheric Sciences, 74, 1705–1719, https://doi.org/10.1175/JAS-D-16-0224.1, 2017.

Pruppacher, H. and Klett, J.: Microphysics of Clouds and Precipitation, vol. 18, https://doi.org/10.1007/978-0-306-48100-0, 2010.

Schwarzenboeck, A., Shcherbakov, V., Lefevre, R., Gayet, J.-F., Pointin, Y., and Duroure, C.: Indications for stellar-crystal fragmentation in Arctic clouds, Atmospheric Research, 92, 220–228, https://doi.org/10.1016/j.atmosres.2008.10.002, 2009.

Sullivan, S. C., Hoose, C., Kiselev, A., Leisner, T., and Nenes, A.: Initiation of secondary ice production in clouds, Atmospheric Chemistry and Physics, 18, 1593–1610, https://doi.org/10.5194/acp-18-1593-2018, 2018.

Szakáll, M., Kessler, S., Diehl, K., Mitra, S. K., and Borrmann, S.: A wind tunnel study of the effects of collision processes on the shape and oscillation for moderate-size raindrops, Atmospheric Research, 142, 67–78, https://doi.org/10.1016/j.atmosres.2013.09.005, 2014.

Szakáll, M. and Urbich, I.: Wind tunnel study on the size distribution of droplets after collision induced breakup of levitating water drops, Atmospheric Research, 213, 51–56, https://doi.org/https://doi.org/10.1016/j.atmosres.2018.05.007, 2018.

Takahashi, T.: High ice crystal production in winter cumuli over the Japan Sea, Geophysical Research Letters, 20, 451–454, https://doi.org/10.1029/93GL00613, 1993.

Takahashi, T., Nagao, Y., and Kushiyama, Y.: Possible High Ice Particle Production during Graupel–Graupel Collisions, Journal of the Atmospheric Sciences, 52, 4523–4527, https://doi.org/10.1175/1520-0469(1995)052<4523:phippd>2.0.co;2, 1995.

Theis, A., Szakáll, M., Diehl, K., Mitra, S. K., Zanger, F., Heymsfield, A., and Borrmann, S.: Vertical Wind Tunnel Experiments and a Theoretical Study on the Microphysics of Melting Low-Density Graupel, Journal of the Atmospheric Sciences, 79, 1069–1087, https://doi.org/10.1175/jas-d-21-0162.1, 2022.

Vardiman, L.: The Generation of Secondary Ice Particles in Clouds by Crystal–Crystal Collision, Journal of the Atmospheric Sciences, 35, 2168–2180, https://doi.org/10.1175/1520-0469(1978)035<2168:tgosip>2.0.co;2, 1978.

Vázquez-Martín, S., Kuhn, T., and Eliasson, S.: Shape dependence of snow crystal fall speed, Atmospheric Chemistry and Physics, 21, 7545–7565, https://doi.org/10.5194/acp-21-7545-2021, 2021.

https://doi.org/10.5194/egusphere-2023-1074
Preprint. Discussion started: 6 June 2023

von Terzi, L., Neto, J. D., Ori, D., Myagkov, A., and Kneifel, S.: Ice microphysical processes in the dendritic growth layer: a statistical analysis combining multi-frequency and polarimetric Doppler cloud radar observations, Atmospheric Chemistry and Physics, 22, 11 795–11 821, https://doi.org/10.5194/acp-22-11795-2022, 2022.

Weitzel, M., Mitra, S. K., Szakáll, M., Fugal, J. P., and Borrmann, S.: Application of holography and automated image processing for laboratory experiments on mass and fall speed of small cloud ice crystals, Atmospheric Chemistry and Physics, 20, 14 889–14 901, https://doi.org/10.5194/acp-20-14889-2020, 2020.